# On the Long-Term Performance of Solitary Wave-Based Transducers for Nondestructive Evaluation Applications

**Hoda Jalali**
Laboratory for Nondestructive Evaluation and Structural Health Monitoring Studies,
Department of Civil and Environmental Engineering,
University of Pittsburgh,
Pittsburgh, PA 15261
e-mail: hoj14@pitt.edu

**Piervincenzo Rizzo**[1]
Laboratory for Nondestructive Evaluation and Structural Health Monitoring Studies,
Department of Civil and Environmental Engineering,
University of Pittsburgh,
Pittsburgh, PA 15261
e-mail: pir3@pitt.edu

*A nondestructive evaluation (NDE) technique based on highly nonlinear solitary waves (HNSWs) has been developed recently by a few groups worldwide. The technique is based on the propagation and detection of these waves along a one-dimensional monoperiodic array of spherical particles in which one end of the array is in contact with the material/structure to be inspected, and the particle at the opposite end induces the waves by means of a mechanical impact. Several studies have demonstrated that the dynamic interaction between the waves and the element to be evaluated is dependent on the geometric and mechanical properties of the structure, and such dependency can be monitored by sensing the waves reflected at the interface between the array and the structure. This NDE technique is typically performed by using the so-called HNSW transducer. The term transducer indicates a portable device that consists of a monoperiodic array of particles, a device to trigger the waves, and a sensing element to detect the waves. In the study presented in this article, the long-term performance of three transducers was investigated by placing them above a test object whose mechanical and geometric properties were left constant for a week while the transducers triggered and detected thousands of waves. Any variability of the waves was quantified by extracting simple features such as amplitude, time of flight, and cross-correlation. To investigate the cause of variabilities, 16 measurements were captured with short videos at ~1000 fps. The results of the study demonstrate that the traveling time of the solitary waves is the most reliable parameter for long-term monitoring with the lowest variability and the least susceptibility to physical changes within the array. In addition, the findings of this study allow the framing of a valid strategy to improve the design of the transducers in order to make the HNSW-based technique suitable for long-term monitoring.*
[DOI: 10.1115/1.4054391]

*Keywords: nondestructive evaluation, highly nonlinear solitary waves, high-speed video processing, diagnostic feature extraction, elastic wave, materials testing, sensors*

## 1 Introduction

Highly nonlinear solitary waves (HNSWs) are lumps of acoustic energy that can propagate in nonlinear systems such as monoperiodic arrays of elastically interacting spheres, sometimes indicated as granular crystals, under zero or weak static compression [1,2]. The nonlinearity originates from the Hertzian contact between adjacent particles [3–5], according to

$$F = A\delta_+^{3/2} \tag{1}$$

Here, $F$ is the contact force between two adjacent particles, $\delta$ is the deformation of the diameter connecting the centers of the interacting particles, and $A$ is the contact stiffness coefficient. In Eq. (1), the subscript + denotes the operator max ($\delta$, 0), which implies that granular crystals do not support tensile force between the particles when they are separated from each other (tensionless contact between the particles).

Compared to linear elastic waves propagating in continuous media, HNSWs present unique properties. For example, they support a high level of acoustic energy within a finite spatial wavelength of five particle diameters, and their propagation speed depends nonlinearly on their amplitude [2,5]. In addition, properties such as wavelength, amplitude, and speed can be tuned without electronic equipment, but by simply adding static precompression on the array or by varying the material and diameter of the particles. The tunability makes the use of HNSWs appealing in those engineering applications such as nondestructive evaluation (NDE) and structural health monitoring (SHM). The scheme of an HNSW-based NDE/SHM is rather straightforward. One end of an array of identical spheres such as the one shown in Fig. 1 is in dry-point contact with the structure to be inspected/monitored. The top particle of the chain is lifted and released to create a mechanical impact that triggers the formation of a solitary pulse, hereinafter referred to as the incident solitary wave (ISW). The ISW propagates through the array, is detected using a sensing system that may or may not be embedded in the chain, and then reaches the surface of the structure. Here, part of the acoustic energy is reflected, giving rise to one or more reflected solitary waves, typically referred to as the primary and the secondary reflected solitary waves (PSW and SSW). These reflected waves are then detected by the same sensing system. Several NDE/SHM applications [6–23] demonstrated that the number, amplitudes, and travel time of the reflected waves depend upon several factors, including the mechanical and geometric characteristics of the structure. For instance, Yang et al. showed numerically, analytically, and experimentally that the amplitude and the arrival time of the reflected waves from the interface of a large thin plate depend on the plate thickness, particles size, and the distance from the plate boundaries [6]. Cai et al. reported that the geometric and mechanical properties of a slender beam and the thermal stress applied to the beam affect the reflected solitary wave features [7]. Kim et al. investigated numerically and

[1]Corresponding author.
Manuscript received October 22, 2021; final manuscript received April 14, 2022; published online May 10, 2022. Assoc. Editor: Wieslaw Ostachowicz.

experimentally that solitary waves can be used to detect delamination in a carbon fiber-reinforced polymer composite plate [8]. A numerical study by Schiffer and Kim showed that solitary waves are effective in evaluating the directional elastic parameters of composites [9]. This solitary-wave-based NDE technique was also proposed to assess the quality of adhesive joints [10], monitor cement hydration [11], detect subsurface voids [12], estimate the modulus of elasticity of materials [14], and infer the internal pressure of tennis balls [15,16], just to mention a few. Recently, the authors applied the technique to monitor localized corrosion in steel plates [22,23]. They showed numerically and experimentally that the amplitude and the time of flight of the reflected solitary waves at the interface between the chain and the plate are dependent on the presence of corrosion.

The assembly of the one-dimensional (1D) array shown in Fig. 1 is embraced by a rigid frame, surmounted by an electromagnet designed to lift and release the top particle (the striker), and completed by a sensing element within an array, which can be denoted as the solitary-wave-based transducer, hereinafter simply the transducer. The effectiveness of the design of this transducer was proven by Rizzo and collaborators in several NDE/SHM-based applications [15–18,21–23] and was recently integrated with the development of a wireless module that enables the remote implementation of the technique [24]. However, the long-term performance in terms of repeatability and sensitivity of the transducers was never investigated. The study presented in this article aims at filling this gap of knowledge, i.e., examining long-term repeatability. Three transducers were assembled and placed in contact with a bilayer system made of a metallic plate and an optical table. The transducers were activated continuously for nearly a week during which over 4000 measurements were taken. To investigate any variability intrinsic to the design of the transducers, the characteristics of the plate were left identical. In addition, a few measurements were observed with the aid of two high-speed cameras operating at 960 fps. The videos were processed using computer vision techniques to identify possible vibration/tilting in the components that might affect the repeatability of the measurements.

This paper is organized as follows. Section 2 presents the setup of the experiment. Section 3 describes the discrete element modeling, developed by the authors, to predict the characteristics of solitary waves in monoperiodic arrays of particles of any size and any material. Section 4 describes the algorithms implemented to process the high-speed videos collected during the experiments. Section 5 discusses the results of the experiment and compares them to the numerical prediction. Section 6 ends the paper with some concluding remarks and suggestions for refining the design of the transducers and for the future development of transducers for NDE and SHM applications based on solitary waves.

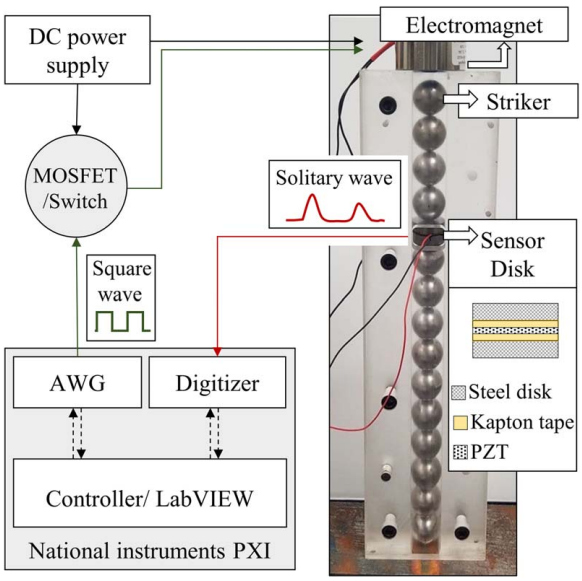


**Fig. 1 Schematics and photo of the solitary wave transducer for NDE/SHM applications**

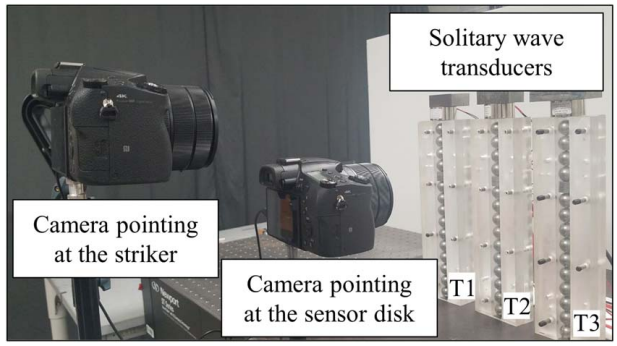


**Fig. 2 Photo of the experimental setup in which two high-speed cameras pointed at the striker and the sensor disk of transducer T2**

## 2 Experimental Setup

Three identical solitary wave transducers, T1, T2, and T3, were assembled in the laboratory. They are shown in Fig. 2. Each transducer contained 14 spheres, one sensor disk, and a commercial electromagnet. The spheres were 19.05 mm in diameter and 28.2 g in mass. All the particles except the striker were stainless steel (type 440 C). The electromagnet was placed 4 mm above the ferromagnetic striker. Each sensor disk was the assembly of a lead zirconate titanate (PZT) wafer in between two 19.05 mm diameter, 6.05 mm thick stainless-steel (type 440 C) disks. The PZT was insulated from the metal using Kapton tape. The mass of each disk was 29 g (in T1 and T3) and 30 g (in T2). As noted in past studies, particles with different mass than the beads of the array give rise to spurious pulses and reflections that may be detrimental for NDE applications.

A National Instruments PCI eXtensions for Instrumentation (PXI) running under LabView was used to control the transducers. The function generator of the PXI sent square waves to a MOSFET also connected to a direct current power supply. The MOSFET acted as a switch to power the electromagnet at intervals selected by the user. When active, the electromagnet lifted the striker that was then released once the electromagnet was powered off. The free-fall of the striker caused the mechanical impact that triggered the generation of the incident wave. The ISW propagated through the chain, interacted with the semi-bulky material in point contact with the chain, and was reflected back. Both the ISW and the PSW were detected by the sensor disk positioned five particles away from the top of the chain. The disk was connected to the digitizer of the PXI. The waves were digitized and stored at a sampling rate of 8 MHz.

The three transducers were positioned on a 609.6 mm × 609.6 mm × 6.35 mm steel plate, located above an optical table. The plate was monitored continuously for nearly a week. Ten measurements were taken every 20 min for a total of 4320 measurements. Shorter intervals would have been possible. However, the commercial electromagnets could have suffered from overheating if used more often. As the plate was not subjected to any type of damage, the setup was instrumental to study the long-term performance of the transducers.

The experimental setup was completed with two high-speed cameras operating at 960 fps. The cameras were pointed at the striker and at the sensor disk of transducer T2, respectively, as shown in Fig. 2. The primary scope was to observe the physical movement of the striker and to detect any oscillation of the sensor disk. Sixteen strikes were recorded using a remote shutter.

## 3 Discrete Element Modeling

To interpret the experimental results, a discrete element model previously developed by the authors [22,23] was used. The model simulates the propagation of solitary waves in granular chains and their interactions with adjacent media. The chains shown in Figs. 1 and 2 were simulated as a series of point masses connected by nonlinear axial connectors. The connectors were defined based on the Hertzian contact model (Eq. (1)). For a chain of $N$ identical spheres, the equation of motion of each particle is

$$m\ddot{u}_i = A_{i-1,i}[u_{i-1}-u_i]_+^{3/2} - A_{i+1,i}[u_i-u_{i+1}]_+^{3/2} + \gamma_{i-1,i}[\dot{u}_{i-1}-\dot{u}_i][u_{i-1}-u_i]_+ - \gamma_{i+1,i}[\dot{u}_i-\dot{u}_{i+1}][u_i-u_{i+1}]_+ + mg \tag{2}$$

where $m$ represents the particle mass, $g$ represents the gravitational acceleration, $u_i$ and $\dot{u}_i$ represent the displacement and the velocity of the $i$th particle, respectively. Additionally, $u_{N+1}$ represents the displacement of the monitoring media at the contact point. Energy dissipation was also considered in the model with different dissipation coefficients ($\gamma$). The coefficient $A_{i,i+1}$ is the contact stiffness between the $i$th and the $i$+1th particles, defined as

$$A_{i,i+1} = \begin{cases} \dfrac{E_p\sqrt{2R}}{3(1-\nu_p^2)} & i = 1{:}N-1, \\ \dfrac{4\sqrt{R}}{3}\left[\dfrac{(1-\nu_p^2)}{E_p} + \dfrac{(1-\nu_m^2)}{E_m}\right] & i = N \end{cases} \tag{3}$$

According to Eq. (3), the stiffness constant is a function of particles radius $R$, the Poisson's ratio $\nu$, and the Young's modulus $E$ of the particles and the monitoring media. The subscript p indicates the properties associated with the particles, whereas the subscript m indicates the monitoring media.

In the present model, the chain consisted of 15 particles which were 19.05 mm in diameter, and their mechanical properties were $E = 200$ GPa and $\nu = 0.3$. The model was used to investigate the interaction of solitary waves with a half-infinite media with different Young's modulus values. The results were used to associate Young's modulus values of the monitoring media with the solitary wave features. Therefore, the model allows us to infer Young's modulus based on the experimental solitary waves features. The Poisson's ratio was fixed at 0.3, as this parameter does not affect the reflected solitary waves significantly. The impact of the striker was simulated by setting the initial velocity $v_0$ of the first particle to a value equal to $v_0 = (2gh)^{1/2}$, where $h$ represents the striker falling height in the transducers.

The dynamic response of the system was obtained by solving the nonlinear equations of motion in MATLAB using the solver ode45. The solitary wave profile at the sensor particle was obtained by averaging the interaction forces between the sensor particle and its adjacent particles. Further details about the model can be found in Refs. [22,23] and are not reported here for the sake of space.

## 4 Video Processing

As said in the Introduction, the motions of the striker and the sensor disk embedded in T2 were analyzed using two video processing algorithms, respectively, implemented in MATLAB. The flowchart of the two algorithms is shown in Figs. 3 and 4, respectively. For the striker (Fig. 3), each video was fragmented into individual frames. Each frame was de-noised with the Wiener filter [25] using a function embedded in MATLAB. Figure 5 shows the noise reduction in one video frame using the Wiener filter with different Gaussian noise variances ($\sigma$). Then, object tracking was performed by detecting the two brightest areas of the striker using the image intensity thresholding. These brightest areas are shown with circles in Fig. 3, and they are the reflections of the light used to illuminate T2. The centroid of the two areas was found in each frame and tracked.

For the sensor disk (Fig. 4), each video was fragmented into individual frames, and each frame was rotated 3 deg clockwise to adjust the image orientation. The motion of the disk was tracked using the Canny edge detection technique [26], also embedded in MATLAB. The results of the application of Canny edge detection to a frame are presented in Fig. 4. Then, the horizontal sensor edges were extracted (shown in Fig. 4), and the sensor centerline was detected as the middle line passing through the sensor horizontal edges. Using this algorithm, the position of the sensor center was found in each image frame, and the sensor's relative position was obtained by finding the differences between subsequent frames.

## 5 Results and Discussion

**5.1 Repeatability: Analyzing the 6-Day Test Results.** Figure 6 presents the mean of all the 4320 solitary waves recorded by each transducer. The incident and the reflected waves are clearly visible. The peak amplitude of the ISW was 4.97 V, 4.73 V, and 4.24 V, for T1, T2, and T3, respectively, which means that the amplitude of T3 was about 17% lower than T1. These discrepancies could have many concurrent causes: slight differences in the falling height of the striker, differences in energy loss due to the friction with the inner wall, different dielectric constants of the PZTs, differences in the manual assembly of the disks, slight rotations of the disks with respect to the longitudinal direction of the wave. As most, if not all, of these causes are difficult to control manually, the outcome is that the amplitude of the waves should not be considered as a damage-sensitive feature for NDE/SHM applications, but normalization is suggested. In addition, the incident wave is not expected to be influenced by the properties of the adjacent material.

Figure 6(*a*) shows a negative voltage spike trailing the incident wave. Although its origin is unclear, it could be related to a temporary lack of static compression on the PZT or a flaw in the assembly of the sensor disk. In all three transducers, the ISW is trailed by a small hump, which is caused by the Hertzian contact between the spherical particle and the disk-shaped sensor. It was described by the authors [23] that this small pulse is the result of the rebound between the sensor disk and the adjacent particles as the contact

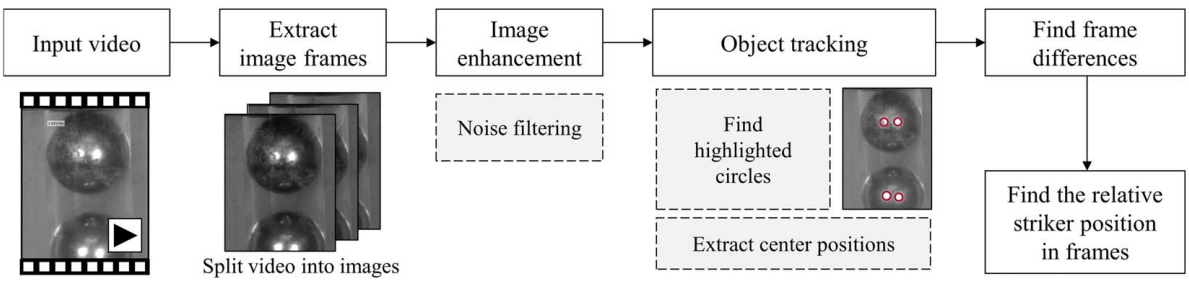


**Fig. 3 Video processing algorithm used to track the striker**

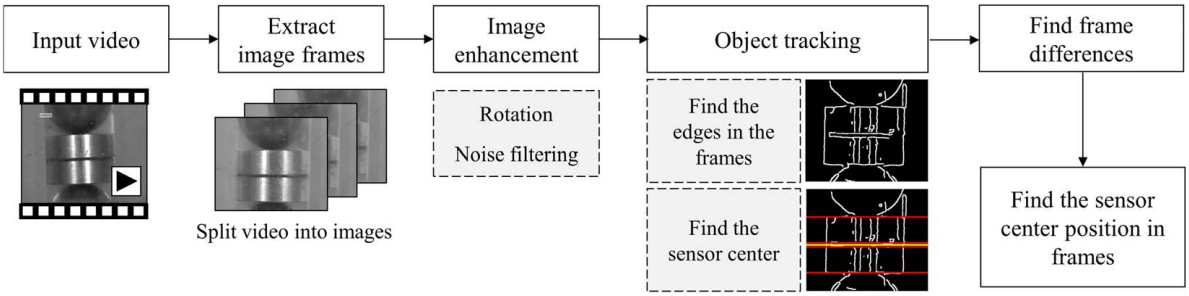


**Fig. 4 Video processing algorithm used to detect the vibrations of the sensor disk**

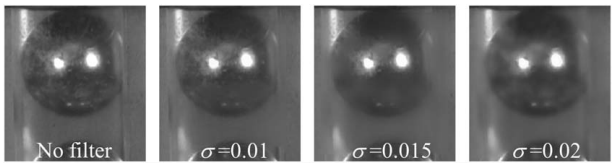


**Fig. 5 Image noise reduction using the Wiener filter with different Gaussian noise variances ($\sigma$)**

stiffness between the sensor disk and the adjacent spheres is higher than the contact stiffness between two spheres. Therefore, the solitary wave propagation speed locally increases at the sensor disk. As the ISW passes through the sensor disk and arrives at the next particle, the disk and the particle separate, yielding to a momentary zero interaction force at the sensor disk. Then, owing to its higher momentum, the sensor disk strikes the following particle again, yielding to the small hump.

The amplitude of the reflected wave was also not the same across the three transducers. Besides the reasons mentioned for the striker, the variations seen for the PSW are to be attributed to small variations of the boundary conditions under the plate, i.e., around the point of contact between the chain and the plate.

Owing to the variabilities detected in Fig. 6, it is important to identify features that prove to be independent from transducer-to-transducer difference and dependent only on the mechanical and geometric properties of the structure to be inspected or monitored over time. Four wave characteristics were considered, namely the amplitude of the incident wave, the time of flight, the normalized amplitude, and the correlation coefficient. The time of flight is the time delay at the sensor disk between the incident and the reflected wave. The normalized amplitude, hereinafter referred to as the amplitude ratio, is the ratio between the amplitude of the reflected wave to the amplitude of the incident wave. Finally, the correlation coefficient, defined as [27]

$$r = \frac{\sum_i (x_i - \bar{x})(y_i - \bar{y})}{\sqrt{\sum_i (x_i - \bar{x})^2 \sum_i (y_i - \bar{y})^2}} \tag{4}$$

measures the similarity between two time waveforms, one of which is a reference signal. In Eq. (4), $x_i$ and $y_i$ are the $i$th values of the two signals, and $\bar{x}$ and $\bar{y}$ are the mean value of the two signals. The correlation coefficient is equal to 1 if the two signals are identical, 0 if they are completely uncorrelated, and $-1$ if they are anti-correlated. In addition, the ISW correlation coefficient and the PSW correlation coefficients were determined by comparing segments of signals that isolate the ISW and the PSW.

Figure 7 presents the values of the features extracted for each transducer. Each data point represents the average of the 10 recordings collected every 20 min. Overall, the features do not show any trend in agreement with the fact that the properties of the plate remained constant. The following additional considerations can be made. The amplitude of the ISW varied visibly within the same transducer as much as 25% (T1). The time of flight is the most repeatable feature, and the coefficient of variation is comprised between 2% and 3%. As the time of flight has the least variability, it can be considered the most reliable parameter for solitary-wave-based NDE applications. The values of the amplitude ratio within each transducer are scattered and the associated coefficient of variation ranges between 12% and 13%. Such variation is caused by the random occurrence of twin reflected solitary waves, as will be discussed later in Sec. 5.3. According to Ref. [15], the twin reflected

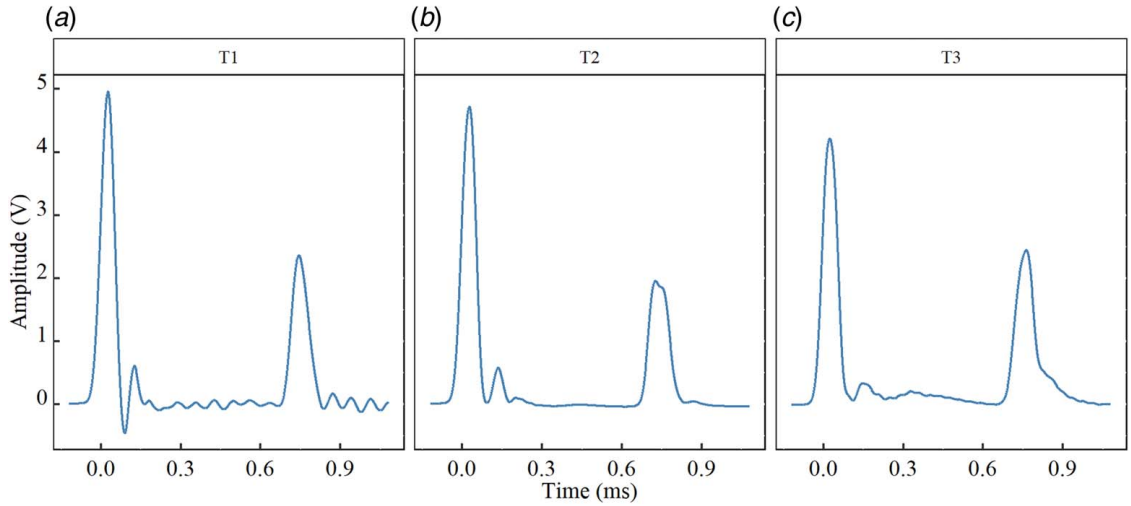


**Fig. 6 Experimental time waveforms obtained by averaging the single waveforms collected throughout the whole experiment: (*a*) Transducer 1, (*b*) Transducer 2, and (c) Transducer 3**

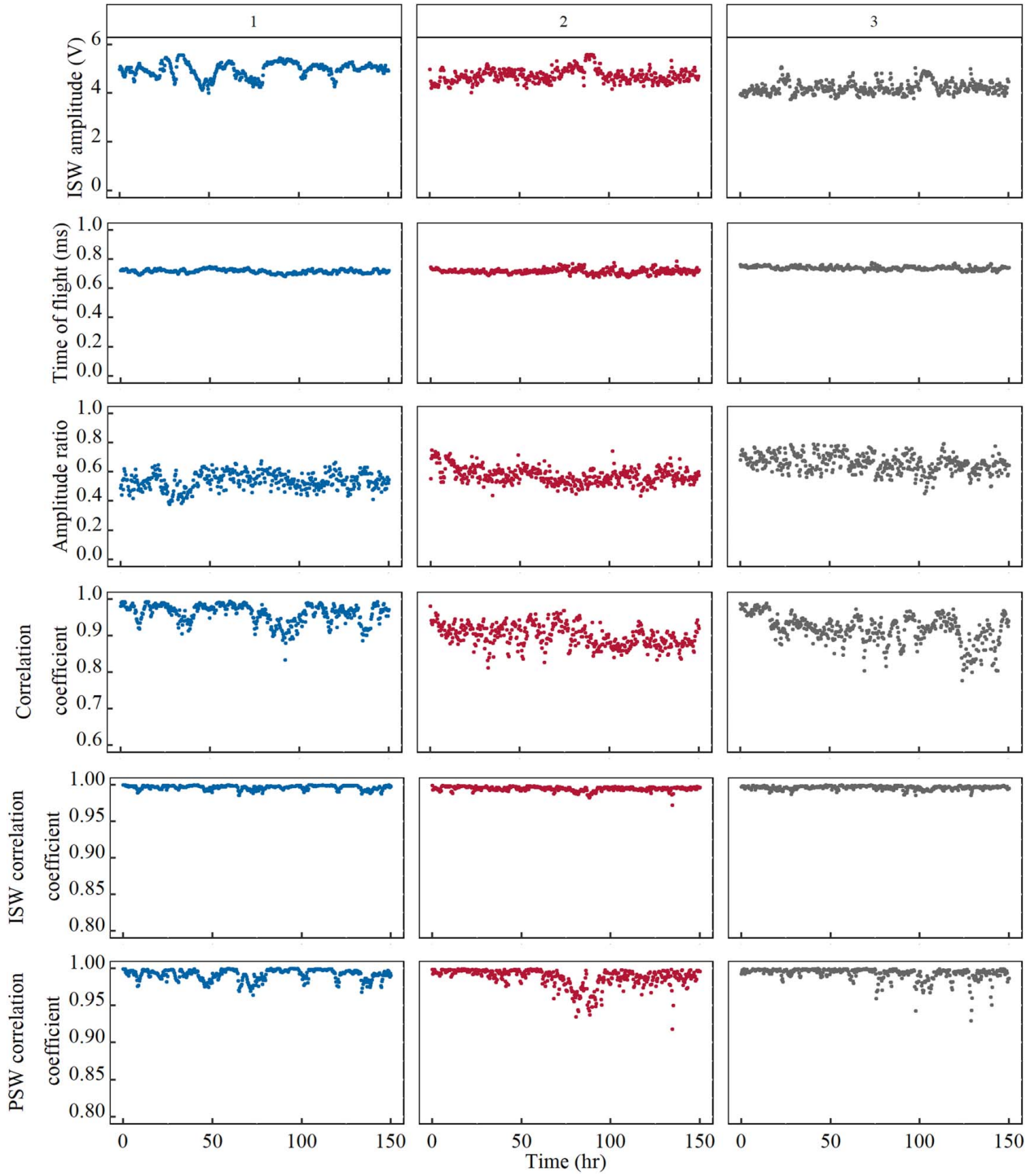


**Fig. 7 The solitary wave features extracted from the time waveforms recorded with the sensor disk. Each dot represents the average value of the ten measurements collected every 20 min. (Left column) Transducer 1, (Center column) Transducer 2, and (Right column) Transducer 3.**

**Table 1 Time waveforms analysis**

| Transducer | Time of flight (ms) | Amplitude ratio | Correlation coefficient | ISW correlation coefficient | PSW correlation coefficient |
|---|---|---|---|---|---|
| 1 | 0.720 | 0.54 | 0.961 | 0.997 | 0.992 |
| 2 | 0.720 | 0.58 | 0.901 | 0.995 | 0.988 |
| 3 | 0.737 | 0.66 | 0.917 | 0.996 | 0.993 |

Note: Average value of the time of flight, amplitude ratio, correlation coefficient, ISW correlation coefficient, and PSW correlation coefficient associated with the three solitary wave transducers.

**Table 2 Comparison between the statistical metrics of the time of flight obtained from the peak-to-peak method and the correlation analysis between the ISW and the PSW**

| | Peak-to-peak method | | | Correlation method | | |
|---|---|---|---|---|---|---|
| Time of flight statistics | Transducer 1 | Transducer 2 | Transducer 3 | Transducer 1 | Transducer 2 | Transducer 3 |
| Mean | 0.717 | 0.717 | 0.740 | 0.723 | 0.713 | 0.734 |
| Standard deviation | 0.013 | 0.024 | 0.014 | 0.012 | 0.017 | 0.012 |

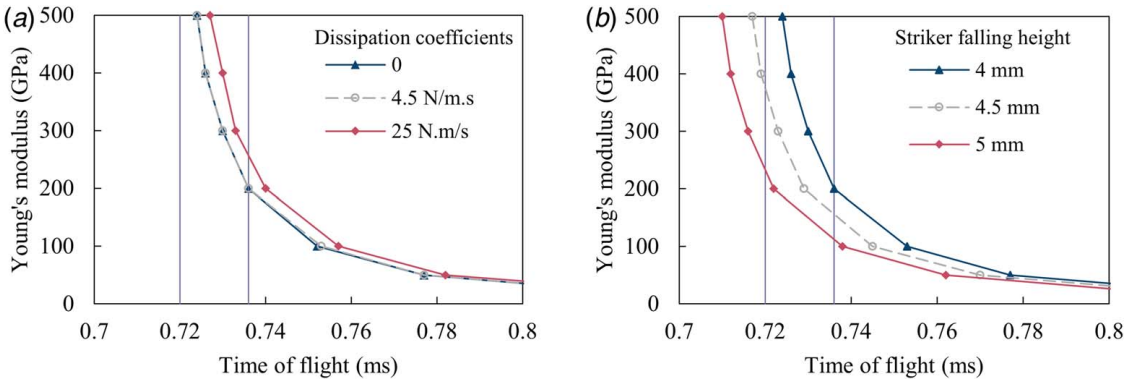


**Fig. 8 Numerical relationship between the elastic modulus of the plate modeled as a semi-bulky material and the time of flight associated with the primary reflected wave: (*a*) Striker fall equal to 4 mm and different dissipation coefficients and (*b*) dissipation coefficient equal to 4.5 N/m.s and different striker falling heights**

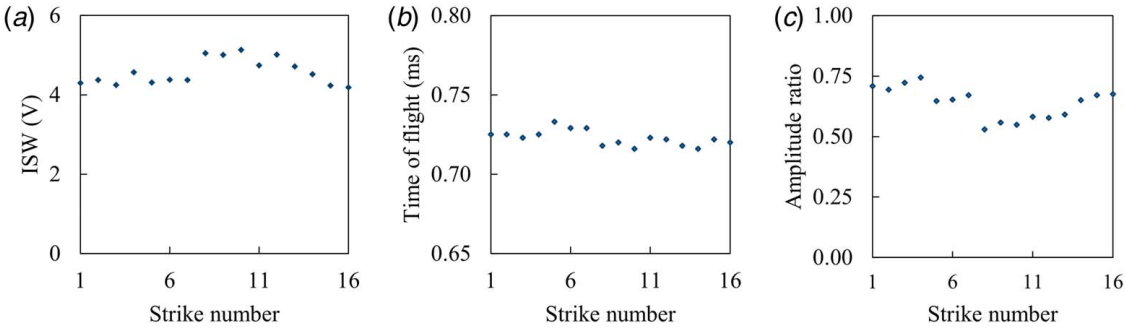


**Fig. 9 Analysis of the 16 videos collected with the two high-speed cameras. Solitary wave features extracted from the time waveforms collected with the sensor disk: (*a*) Peak amplitude of the incident wave, (*b*) time of flight associated with the primary reflected wave, and (*c*) normalized amplitude of the reflected wave.**

solitary waves could be caused by low static precompression in the chain. Striker motions and sensor vibrations could also be the contributing factors to the variations in the amplitude of the incident wave. For the correlation coefficients, the analysis of the whole time waveforms and the analysis of the individual pulses, i.e., ISW and PSW, were carried out. The coefficient related to the whole waveforms spanned between 0.8 and 1. The range is much narrower when the individual pulses were considered. The incident wave remained nearly identical in shape throughout the experiment, whereas the coefficient of the reflected wave was as low as 0.9 when a twin wave was generated at the interface. For instance, the lower PSW correlation coefficients obtained from the second transducer between 70 h and 100 h after the start of the test are associated with twin PSWs.

The average value of the time of flight, amplitude ratio, and correlation coefficients relative to each transducer are presented in Table 1. Transducers 1 and 2 are very similar to each other whereas transducer 3 had a slightly higher average time of flight and amplitude ratio values. As discussed earlier, such small discrepancies can be attributed to different energy losses due to friction with the frames or other assembly differences that are difficult to control. Table 1 shows that the average ISW correlation coefficient was higher than 0.995 for all the transducers, showing the repeatability of the generated ISWs over the experiment.

It is known that the calculation of the time delay between two signals can be more accurate by computing the cross-correlation

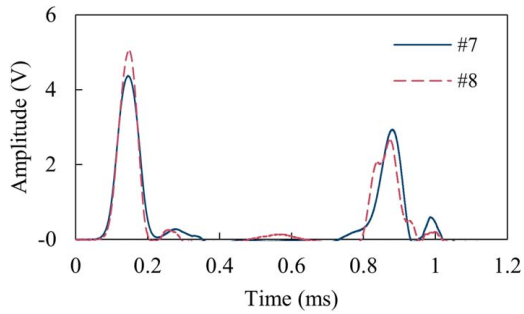


**Fig. 10 Time waveforms measured by the sensor disk associated with strikes number 7 and 8**

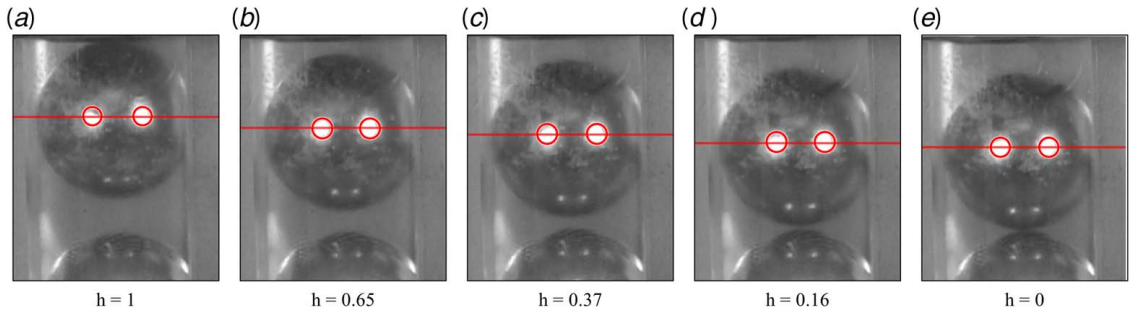


**Fig. 11 Snapshots of the striker particle relative to one of the 16 striker falls. The value of *h* indicate the relative position of the striker.**

between the two signals. For the experimental time waveforms observed in this study, the peak-to-peak method and the cross-correlation yield to very similar results as shown in Table 2. The table presents a comparison between the mean and the standard deviation of the time of flight obtained from the two methods at each transducer. Only a 1% difference was observed between the correlation method instead of the peak-to-peak method. However, the standard deviation values are slightly lower in the case of using the correlation method, which implies lower variability within the time of flight values associated with each group. This is caused by the fact that the correlation analysis considers the entire shape of the ISWs and the PSWs rather than the peaks, which results to lower susceptibility to noises in the signals and possible errors originating from the flaw in the manufacturing the sensor disks and their vibrations, discussed later.

**5.2 Estimating the Plate Young's Modulus: Using Solitary Wave Features.** To explain how the technology could be used for the noninvasive characterization of materials, this section describes the approach to estimating the elastic modulus of the plate using the experimental data discussed in Sec. 5.1. First, a model of the setup was created using the discrete element model presented in Sec. 3. The plate placed on an optical table was assumed to behave as a semi-infinite solid. Noteworthy the model is not strictly accurate, as the transducers sit on a bilayer system one of which has a rectangular grid of tapped holes. The density and the Poisson's ratio of the body were assumed to be equal to 7800 kg/m$^3$ and 0.3, respectively. The solitary wave features were obtained for different values of the Young's modulus, which is the main factor affecting the solitary wave features [14].

Figure 8 presents the numerically predicted relationship between the elastic modulus and the time of flight. Six cases were modeled. Three models (Fig. 8(*a*)) assume a 4-mm free-fall of the striker and dissipation coefficients equal to 0, 4.5 N·m/s, and 25 N·m/s. The remaining models (Fig. 8(*b*)) considered three falling heights, namely, 4 mm, 4.5 mm, and 5 mm with the dissipation coefficient equal to 4.5 N/m·s. The vertical lines overlapped to Fig. 8 identify the experimental average time of flight measured from Fig. 6, namely 0.720 ms (transducers 1 and 2) and 0.737 ms (transducer 3). Both figures demonstrate that the time of flight increases as Young's modulus of the material to be characterized becomes softer. This occurs because the acoustic energy carried by the solitary pulse increases the deformation of the material surface, delaying the rebound of the pulse.

The curves are steeper for stiffer materials, for which a small change in time of flight yields to a large change in the predicted modulus. For example, the 2–3% variability in the experimental measurements of the time of flight seen and discussed in Fig. 7 does not affect the accuracy of the estimated Young's modulus of soft materials (<100 GPa) but may compromise the accurate estimate of stiff materials (>250 MPa). Furthermore, this analysis shows that the characterization of stiff materials requires an accurate

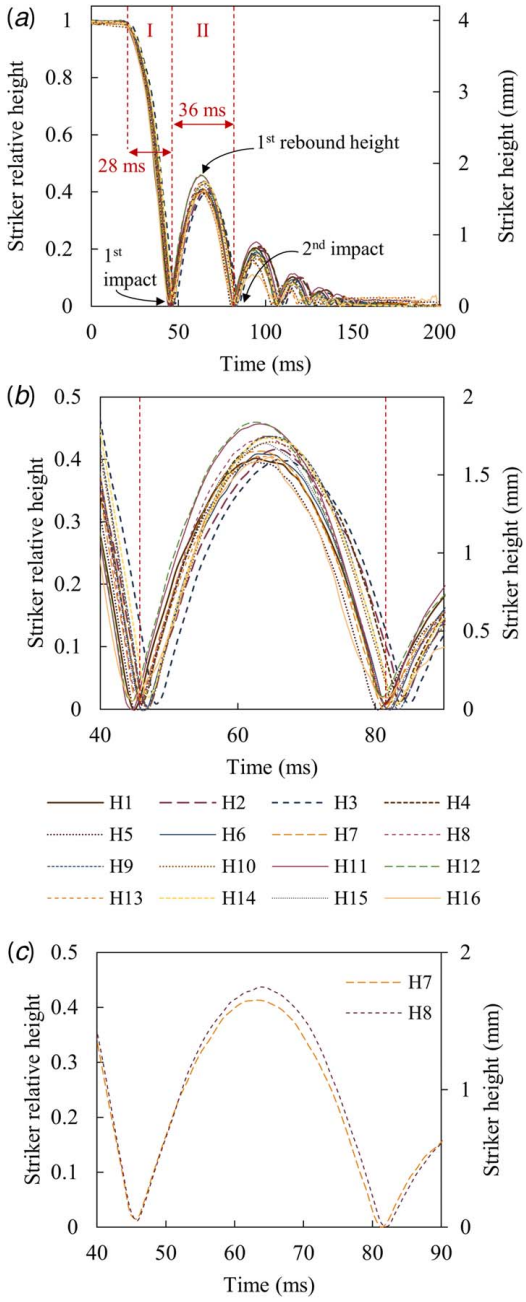


**Fig. 12 Video processing analysis of the striker motion: (*a*) vertical position of the striker for all 16 events for the whole duration of the motion; (*b*) closeup view of the motion relative to the first and the second impacts on the chain; and (*c*) as of (*b*) but relative to strikes number 7 and 8.**

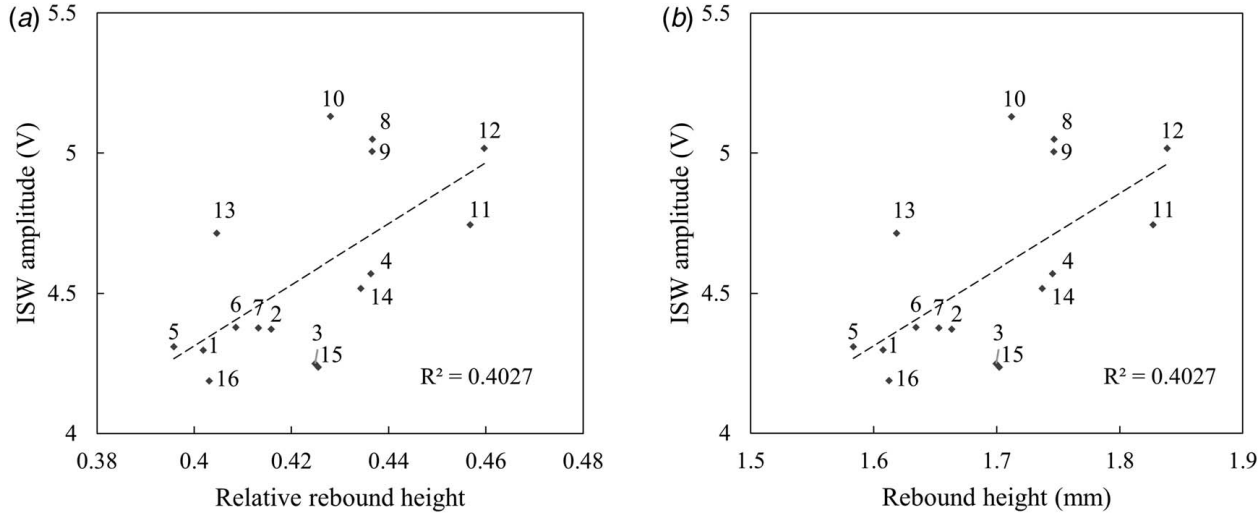


**Fig. 13 Video processing analysis of the striker motion. Peak amplitude of the incident wave recorded with the sensor disk and the corresponding (*a*) relative rebound height and (*b*) rebound height.**

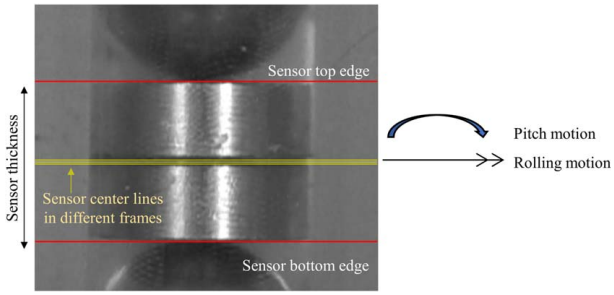


**Fig. 14 Video processing of the sensor disk. Individual frame and pre-processing. The edges and centerlines of the sensor disk identified using the video processing algorithm adopted in this study.**

model and an accurate instrument, because small errors in the measurements may yield large errors in the estimation of the elastic modulus.

Figure 8(*a*) shows that at a given Young's modulus, the time of flight is directly proportional to the energy dissipation consistent with the fact that weaker incident waves travel at a slower speed. However, the effect of dissipation on the time of flight seems to be small. Figure 8(*b*) demonstrates that small differences in the free-fall of the striker have a significant effect on the prediction of the elastic modulus, especially for stiff materials. For example, when the recorded time of flight is 0.737 ms, the elastic modulus associated with the 4 mm falling height is about 100 GPa, but it doubles if the falling height was 5 mm. Figure 8(*b*) shows that larger falls induce faster waves in agreement with the fact that stronger impacts induce higher amplitudes and therefore faster waves.

Under the reasonable assumption that the dissipation was absent or small, the measurement performed with T3 yields an estimated Young's modulus equal to ~ 200 GPa, whereas the estimations performed with T1 and T2 do not match the numerical estimations. Despite 0.737 ms being only 2% higher than 0.720 ms, the difference in the estimation of the modulus is quite significant. To overcome such limitations, the diameter and the material of the particles should be modified in order to shift the gradient of the curves. Assuming that the striker's falling height was 5 mm in transducers 1 and 2 yields to an estimated Young's modulus equal to ~ 220 GPa. Therefore, the lower average time of flight and higher ISW amplitude in transducers 1 and 2 could be caused by a higher striker falling height due to a flaw in the manufacturing or assembly of those transducers.

**5.3 Video Processing Results.** To gain more insights into the dynamics associated with the generation and detection of HNSWs, 16 solitary wave strikes were randomly recorded with the two high-speed cameras and processed with the two video processing techniques discussed in Sec. 2. First, Fig. 9 presents the ISW amplitude, time of flight, and normalized ratio measured from the time waveforms associated with those 16 events. The amplitude of the ISW varied between 4.2 V and 5.1 V, the time of flight varied between 0.707 ms and 0.737 ms, and the normalized amplitude spanned from 0.53 to 0.74. The observations agree with what was discussed in Sec. 5.1. To investigate the step between strikes #7 and #8, which occurred about three hours apart. Figure 10 shows the associated time waveforms. The shape of the two ISWs is identical but the peak amplitude of strike #8 is about 15% higher. The two PSWs are instead different in shape and amplitude.

Figure 11 shows five frames relative to one of the 16 strikes. The position of the striker is shown at different positions, labeled with the parameter $h$. The value equal to 1 identifies the striker in contact with the electromagnet (Fig. 11(*a*)). The value equal to 0 represents the striker in contact with the second particle of the chain (Fig. 11(*e*)). The encircled bright areas were detected using image intensity thresholding. The horizontal lines passing through the center of the circles were used to determine the relative height of the striker. The positions $h = 1$ and $h = 0$ were 72 pixels apart, and given that the striker fall was 4 mm, the camera resolution is 18 pixels per mm, equivalent to 56 $\mu$m. As the frame rate of the cameras was 960 fps, the time intervals between the video frames are about 1 ms. It can be shown that the maximum striker displacement between the video frames which could be missed due to the frame rate limitations is less than 150 $\mu$m.

Figure 12(*a*) shows $h$ as a function of time. The duration of the first fall was about 28 ms, equivalent to the time necessary for a body to fall from a height of 4 mm. The figure reveals that the striker hit the chain about five times, and the time interval between the first and the second hit was about 36 ms, which is much longer than the time of flight of the PSW. This implies that the second impact does not interfere with the propagation of solitary waves that are used for NDE and SHM applications. A closeup view of Fig. 12(*a*) is presented in Fig. 12(*b*) and shows that the first impact of the striker with the second particle of the chain did not occur at the same time in different events. This is because the cameras were manually activated with a remote shutter whereas

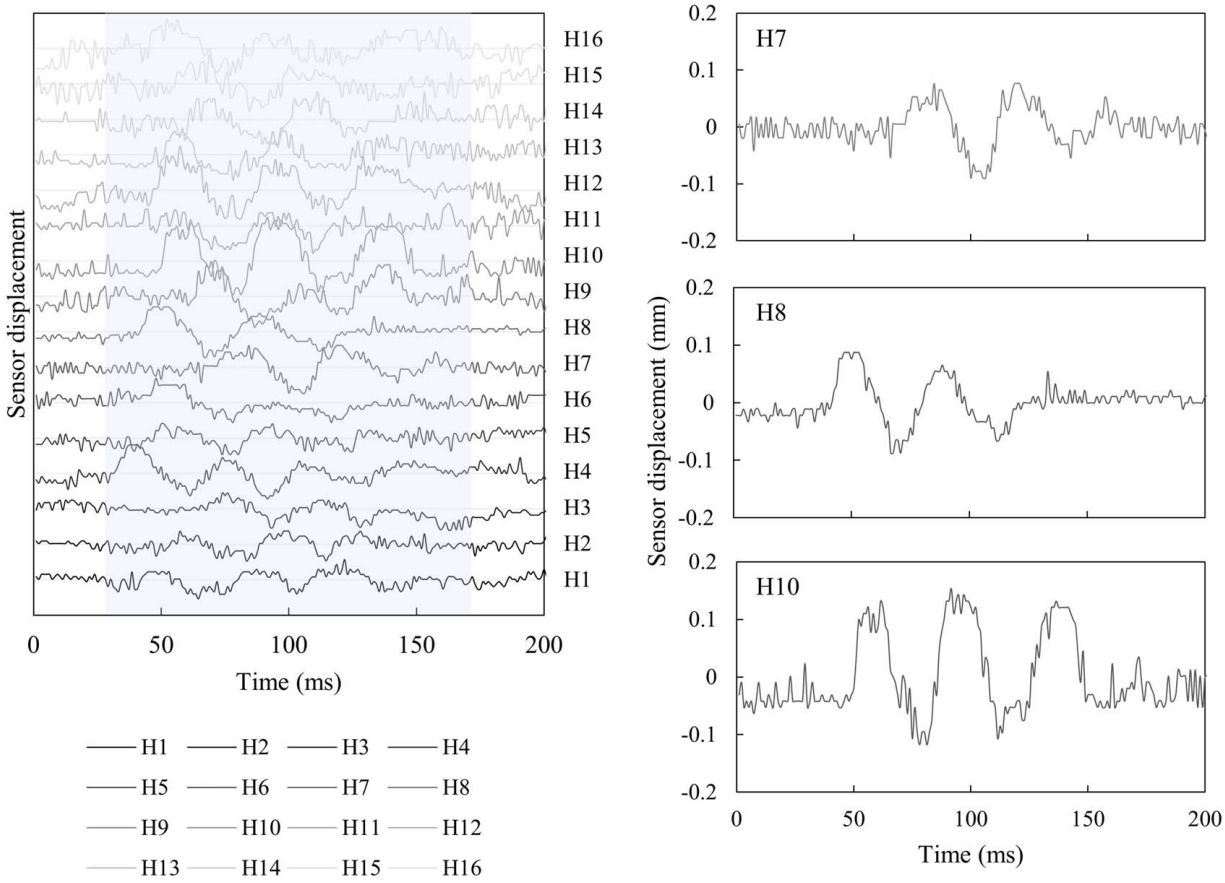


**Fig. 15 Video processing of the sensor disk. (Left column) Time history of the disk vibrations. Note that the position of the sensor centerline was obtained by averaging the position of four horizontal edges associated with the sensor disk. As such, the sensor displacements were discretized in steps of 0.25 pixel. Therefore, the minimum sensor displacement obtained from the videos is about 0.011 mm. (Right column) Close-up view of strikes 7, 8, and 10.**

the electromagnet was controlled by the PXI. Figure 12(*b*) shows also that apparently some impacts never occurred; i.e., there are no data points with $h = 0$. This is because the impact occurred in between two consecutive frames, which are about 1 ms apart. The curves relative to strikes #7 and #8 are presented in Fig. 12(*c*). Surprisingly, the two graphs are quite similar and are therefore unable to provide any insight about the differences noted in Figs. 9 and 10.

To investigate a relationship between the amplitude of the incident wave and the strength of the impact, the peak amplitude of the ISW is plotted against the normalized height of the 1st rebound $h$ (Fig. 13(*a*)) and the 1st rebound height, i.e., the distance between the striker and the second particle of the chain (Fig. 13(*b*)). The labels indicate the strike number while the dashed line represents a linear regression. Overall, the amplitude of the ISW is proportional to the height of the first rebound. However, such dependence is not as evident as expected. As a matter of fact, a closeup view of the graph shows that the strike with the highest amplitude (strike #10) did not correspond with the highest rebound. Conversely, one of the lowest rebounds (strike #13) is not associated with one of the lowest amplitudes. The reasons associated with such discrepancies are unclear and only in part can be associated with the resolution of the videos, for which each pixel represents 56 $\mu$m, equivalent to 0.014 relative rebound height.

In order to investigate the dynamic response of the sensor disk, the edges of the disk (Fig. 14) were tracked during the analysis of each frame. The top and the bottom edge of the disk, shown with horizontal lines, were 273 pixels apart. As the sensor disk (composed of two steel disks, PZT, and Kapton tape) was about 12.4 mm thick, the video resolution was about 22 pixels/mm; i.e., each pixel was 45 $\mu$m. The sensor centerline in each frame was also obtained by finding the middle horizontal line passing through the detected sensor edges. The analysis unveiled that the disk rolled as much as 4 pixels, equivalent to 0.180 mm, whereas there was no evidence of pitch motion.

The left column of Fig. 15 presents a waterfall chart of the rolling vibration in the 16 recorded videos. The oscillations occurred between 50 ms and 150 ms consistent with what observed in Fig. 12. Interestingly, the oscillations seem to have started a few milliseconds after the impact of the striker. As the recordings were started manually, the start of the oscillation varied slightly. The right column of Fig. 15 presents the time waveforms of different strikes H7, H8, and H10. The peak-to-peak amplitudes of the three strikes are different, as well as their arrival. The latter may be caused by asynchronization from strike to strike although we may not exclude that the oscillations are not strictly triggered by the crossing of the solitary wave but rather by a general vibration of the whole transducer generated by the impact of the striker. A cross-comparison between these waveforms and Fig. 13 shows that the largest peak-to-peak amplitude (H10) does correspond to the highest ISW amplitude but not the highest rebound height. It is shown that the magnitude of the sensor vibrations varies in different solitary wave incidences. Despite the rebound heights of the striker for H7 and H8 being nearly identical, and therefore, it can be assumed that the impact force was nearly the same, the oscillations of the sensor disk for the same event are quite different.

Finally, Fig. 16 shows the magnitude of the oscillations sensor vibrations in colors in order to emphasize the differences among the 16 strikes. Figure 17 shows the peak-to-peak sensor displacement obtained from the videos as a function of the associated ISW amplitude. The results confirm that stronger ISW-induced large oscillations.

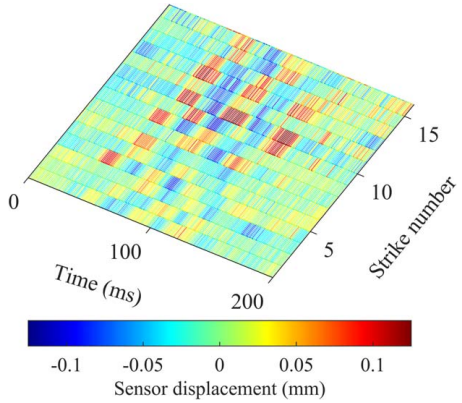


**Fig. 16 The sensor vibrations detected in the videos in color-map format**

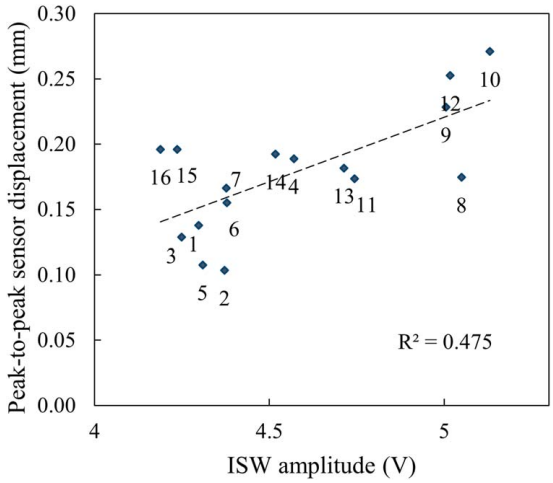


**Fig. 17 Peak-to-peak sensor displacement as a function of the associated incident solitary wave amplitudes**

## 6 Conclusion

This article presents a study on the long-term reliability of a transducer system for the nondestructive evaluation of structures based on highly nonlinear solitary waves. The noninvasive technique is based on the propagation and detection of solitary waves propagating along a monoperiodic array of spherical particles in which one particle of the array is in contact with the material/structure to be inspected. The term transducer indicates a portable device that consists of a monoperiodic array of particles, a device to trigger the waves, and a sensing element to detect the waves. In the study presented in this article, the long-term performance of three transducers was investigated by placing the transducers above a test object monitored for a week while the transducers triggered and detected thousands of waves. The variability of the stress waves, mechanically induced by the impact of the striker, was quantified by extracting simple features such as amplitude and time of flight. In addition, 16 measurements were captured with short videos at ~1000 fps. The results of the study demonstrate that the traveling time of the solitary waves is the most reliable parameter for long-term monitoring with the lowest variability and the least susceptibility to physical changes within the array. When the NDE applications are targeted to the characterization of the material, the results demonstrate that an accurate model of the dynamic interaction between solitary waves and material is needed in order to obtain reliable predictions of the elastic modulus of the material to be characterized. While acoustic leakage in the form of dissipation seems to be non-critical for such predictions, the precise control of the free-fall of the striker and the elastic deformation of the material underneath the chain is pivotal. The fact that the features selected in the study were overall constant, suggesting that the HNSW transducer can be used for damage detection. In addition, the absence of any trend proved that the particles were neither damaged nor subjected to plastic deformation. It is noteworthy that the Hertzian contact formulation described in Eq. (1) describes the force–displacement relationship under elastic deformation and are adequate to describe the propagation of HNSWs without plastic deformation among the particles. When plastic deformation is expected, detailed elastoplastic contact models [28–30] should be considered, to investigate energy dissipation that originates from the plastic deformation in the particles.

The findings of this study suggest revisiting the design of the sensing system and in particular considering valid alternatives to the PZT bonded in between two thick disks.


## Funding Data

- The U.S. National Science Foundation, Grant No. 1809932.


## Conflict of Interest

There are no conflicts of interest.

## Data Availability Statement

The data sets generated and supporting the findings of this article are obtainable from the corresponding author upon reasonable request.

## References


[1] Nesterenko, V. F., 1984, "Propagation of Nonlinear Compression Pulses in Granular Media," J. Appl. Mech. Tech. Phys., **24**(5), pp. 136–148.
[2] Sen, S., Hong, J., Bang, J., Avalos, E., and Doney, R., 2008, "Solitary Waves in the Granular Chain," Phys. Rep., **462**(2), pp. 21–66.
[3] Hertz, H., 1881, "On the Contact of Elastic Solids," Z. Reine Angew. Math., **92**, pp. 156–171.
[4] Johnson, K. L., and Johnson, K. L., 1987, *Contact Mechanics*, Cambridge University Press, Cambridge, UK.
[5] Daraio, C., Nesterenko, V. F., Herbold, E. B., and Jin, S., 2006, "Tunability of Solitary Wave Properties in one-Dimensional Strongly Nonlinear Phononic Crystals," Phys. Rev. E: Stat., Nonlinear, Soft Matter Phys., **73**(2 Pt 2), p. 026610.
[6] Yang, J., Khatri, D., Anzel, P., and Daraio, C., 2012, "Interaction of Highly Nonlinear Solitary Waves With Thin Plates," Int. J. Solids Struct., **49**(13), pp. 1463–1471.
[7] Cai, L., Rizzo, P., and Al-Nazer, L., 2013, "On the Coupling Mechanism Between Nonlinear Solitary Waves and Slender Beams," Int. J. Solids Struct., **50**(25–26), pp. 4173–4183.
[8] Kim, E., Restuccia, F., Yang, J., and Daraio, C., 2015, "Solitary Wave-Based Delamination Detection in Composite Plates Using a Combined Granular Crystal Sensor and Actuator," Smart Mater. Struct., **24**(12), p. 125004.
[9] Schiffer, A., and Kim, T.-Y., 2019, "Modelling of the Interaction Between Nonlinear Solitary Waves and Composite Beams," Int. J. Mech. Sci., **151**, pp. 181–191.
[10] Ni, X., and Rizzo, P., 2012, "Highly Nonlinear Solitary Waves for the Inspection of Adhesive Joints," Exp. Mech., **52**(9), pp. 1493–1501.
[11] Ni, X., Rizzo, P., Yang, J., Katri, D., and Daraio, C., 2012, "Monitoring the Hydration of Cement Using Highly Nonlinear Solitary Waves," NDT&E Int., **52**, pp. 76–85.
[12] Schiffer, A., Alkhaja, A. I., Yang, J., Esfahani, E. N., and Kim, T. Y., 2017, "Interaction of Highly Nonlinear Solitary Waves With Elastic Solids Containing a Spherical Void," Int. J. Solids Struct., **118**, pp. 204–212.
[13] Zheng, B., Rizzo, P., and Nasrollahi, A., 2020, "Outlier Analysis of Nonlinear Solitary Waves for Health Monitoring Applications," Struct. Health. Monit., **19**(4), pp. 1160–1174.
[14] Deng, W., Nasrollahi, A., Rizzo, P., and Li, K., 2016, "On the Reliability of a Solitary Wave Based Transducer to Determine the Characteristics of Some Materials," Sensors, **16**(1), p. 5.
[15] Nasrollahi, A., Rizzo, P., and Orak, M. S., 2018, "Numerical and Experimental Study on the Dynamic Interaction Between Highly Nonlinear Solitary Waves and Pressurized Balls," ASME J. Appl. Mech., **85**(3), p. 031007.
[16] Nasrollahi, A., Lucht, R., and Rizzo, P., 2019, "Solitary Waves to Assess the Internal Pressure and the Rubber Degradation of Tennis Balls," Exp. Mech., **59**(1), pp. 65–77.

[17] Nasrollahi, A., and Rizzo, P., 2018, "Axial Stress Determination Using Highly Nonlinear Solitary Waves," The J. Acoust. Soc. Am., **144**(4), pp. 2201–2212.
[18] Nasrollahi, A., and Rizzo, P., 2019, "Numerical Analysis and Experimental Validation of an Nondestructive Evaluation Method to Measure Stress in Rails," ASME J. Nondestruct. Eval. Diagn. Progn. Eng. Syst., **2**(3), p. 031002.
[19] Singhal, T., Kim, E., Kim, T. Y., and Yang, J., 2017, "Weak Bond Detection in Composites Using Highly Nonlinear Solitary Waves," Smart Mater. Struct., **26**(5), p. 055011.
[20] Schiffer, A., Alia, R. A., Cantwell, W. J., Lee, D., Kim, E., and Kim, T. Y., 2020, "Elastic Interaction Between Nonlinear Solitary Waves in Granular Chains and Composite Beams: Experiments and Modelling," Int. J. Mech. Sci., **170**, p. 105350.
[21] Jalali, H., Zeng, Y., Rizzo, P., and Bunger, A., 2021, "Highly Nonlinear Solitary Waves to Estimate Orientation and Degree of Anisotropy in Rocks," Mater. Eval., **79**(10).
[22] Jalali, H., and Rizzo, P., 2020, "Highly Nonlinear Solitary Waves for the Detection of Localized Corrosion," Smart Mater. Struct., **29**(8), p. 085051.
[23] Jalali, H., and Rizzo, P., 2021, "Numerical Investigation of the Interaction of Highly Nonlinear Solitary Waves With Corroded Steel Plates," Int. J. Mech. Sci., **208**, p. 106676.
[24] Misra, R., Jalali, H., Dickerson, S. J., and Rizzo, P., 2020, "Wireless Module for Nondestructive Testing/Structural Health Monitoring Applications Based on Solitary Waves," Sensors, **20**(11), p. 3016.
[25] Wiener, N., 1964, *Extrapolation, Interpolation, and Smoothing of Stationary Time Series: With Engineering Applications*, Vol. 8, MIT Press, Cambridge, MA.
[26] Canny, J., 1986, "A Computational Approach to Edge Detection," IEEE Trans. Pattern Anal. Mach. Intell., **PAMI-8**(6), pp. 679–698.
[27] Lee Rodgers, J., and Nicewander, W. A., 1988, "Thirteen Ways to Look at the Correlation Coefficient," Am. Stat., **42**(1), pp. 59–66.
[28] Feng, Y., Kang, W., Ma, D., and Liu, C., 2019, "Multiple Impacts and Multiple-Compression Process in the Dynamics of Granular Chains," ASME J. Comput. Nonlinear Dyn., **14**(12), p. 121002 .
[29] Burgoyne, H. A., and Daraio, C., 2014, "Strain-Rate-Dependent Model for the Dynamic Compression of Elastoplastic Spheres," Phys. Rev. E, **89**(3), p. 032203.
[30] Ma, D., and Liu, C., "Contact Law and Coefficient of Restitution in Elastoplastic Spheres," ASME J. Appl. Mech., **82**(12), p. 121006.